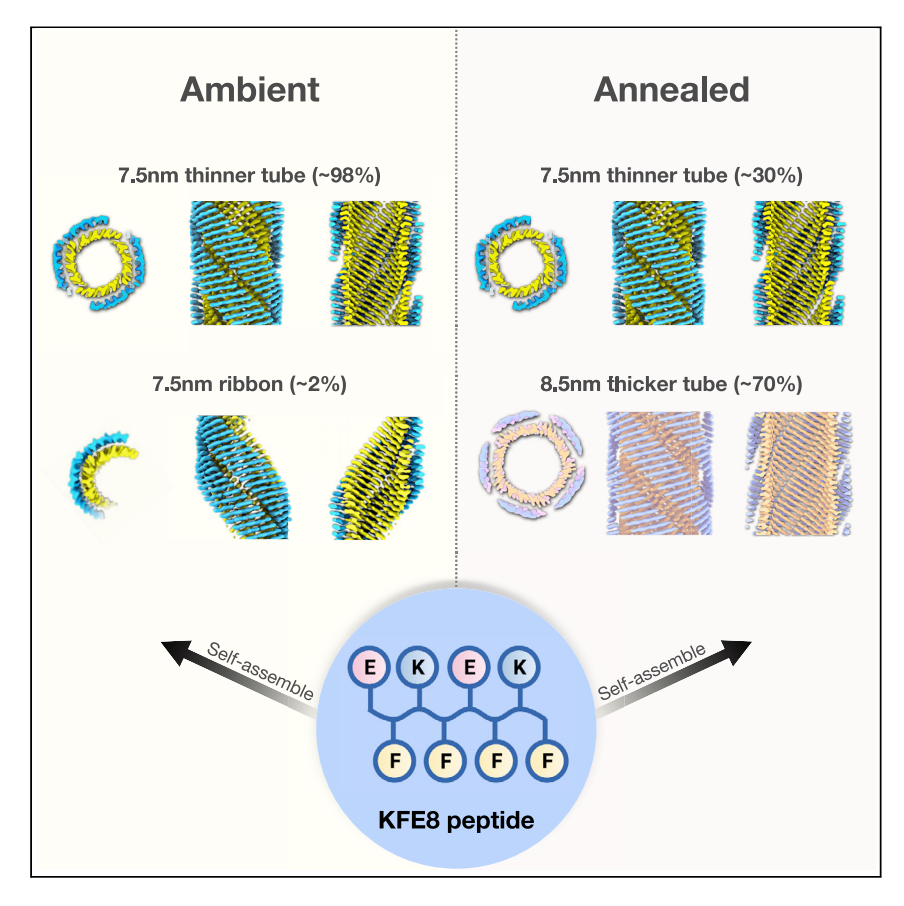
Matter



Article

Deterministic chaos in the self-assembly of β sheet nanotubes from an amphipathic oligopeptide



Peptide assemblies are commonly employed as *in vivo* biomaterials in therapeutic applications; however, limited information is usually available on the structure of the assemblies and its influence on the biological mechanism of action. Cryo-EM is employed here for the structural analysis of assemblies derived from amphipathic β sheet oligopeptide KFE8 at near-atomic resolution. The structure of corresponding filaments depends strongly on assembly conditions. This process may be indicative of a more general phenomenon of chaotic behavior in peptide folding and assembly.

Fengbin Wang, Ordy Gnewou, Shengyuan Wang, Tomasz Osinski, Xiaobing Zuo, Edward H. Egelman, Vincent P. Conticello

egelman@virginia.edu (E.H.E.) vcontic@emory.edu (V.P.C.)

Highlights

Amphipathic peptide KFE8, Ac-FKFEFKFE-NH₂, assembles into ribbons and nanotubes

Cryo-EM reveals that the structures of the filaments depend on assembly conditions

The structures display an unusual arrangement of antiparallel sheet on parallel sheet

The self-assembly of KFE8 may represent an example of deterministic chaos in folding



Matter



Article

Deterministic chaos in the self-assembly of β sheet nanotubes from an amphipathic oligopeptide

Fengbin Wang,¹ Ordy Gnewou,² Shengyuan Wang,² Tomasz Osinski,¹ Xiaobing Zuo,³ Edward H. Egelman,^{1,*} and Vincent P. Conticello^{2,4,5,*}

SUMMARY

The self-assembly of designed peptides into filaments and other higher-order structures has been the focus of intense interest because of the potential for creating new biomaterials and biomedical devices. These peptide assemblies have also been used as models for understanding biological processes, such as the pathological formation of amyloid. We investigate the assembly of an octapeptide sequence, Ac-FKFEFKFE-NH2, motivated by prior studies that demonstrated that this amphipathic β strand peptide self-assembled into fibrils and biocompatible hydrogels. Using high-resolution cryoelectron microscopy (cryo-EM), we are able to determine the atomic structure for two different coexisting forms of the fibrils, containing four and five β sandwich protofilaments, respectively. Surprisingly, the inner walls in both forms are parallel β sheets, while the outer walls are antiparallel β sheets. Our results demonstrate the chaotic nature of peptide self-assembly and illustrate the importance of cryo-EM structural analysis to understand the complex phase behavior of these materials at near-atomic resolution.

INTRODUCTION

Synthetic peptide filaments have been studied for nearly three decades. 1-3 Despite extensive research effort, the design of self-assembling peptides remains largely empirical and is primarily drawn from sequence-structure correlations established from analysis of soluble proteins and discrete oligomers. β sheet filaments were among the first synthetic peptide assemblies to be reported. 4-6 The peptide designs were based on an alternating non-polar/polar residue pattern that biased the sequences toward adoption of an amphipathic β strand conformation. Self-association of β strands through hydrogen-bonding interactions resulted in the formation of cross- β filaments. ⁷⁻⁹ In the case of amphipathic β strand peptides, this process was accompanied by pairwise interaction of β sheets in which the hydrophobic residues were buried at the interface. 10 Thus far, high-resolution structural analysis of designed β sheet assemblies has been limited to solid-state NMR methods, ^{11–13} which cannot easily determine long-range structure. Supramolecular structural parameters have functional importance as they have a significant impact on materials properties, such as liquid crystallinity, gelation, and mechanical response. 14,15 In addition, long-range structure influences the density, symmetry, and spatial availability of bioactive functional groups along the contour length of a filament, and, consequently, the ability of the material to predictably and productively engage in cellular interactions at biointerfaces. In the case of cross-\$\beta\$ filaments, these

Progress and potential

Peptide-based assemblies offer the opportunity to control supramolecular structure through intermolecular interactions that are programmed into the peptide sequence. These biomaterials can be designed to incorporate biofunctionality and biocompatibility that enhances their potential in therapeutic applications. However, the structures of the corresponding assemblies are often not known at near-atomic resolution, which complicates the interpretation of their mechanism of action at the critical cell-biomaterial interface. Here, cryo-EM is employed for the high-resolution structural analysis of assemblies derived from the well-studied amphipathic octapeptide, KFE8. The formation of structurally distinct ribbons and nanotubes is observed when KFE8 is assembled under different conditions. This process is suggestive of chaotic behavior, in which small differences in conditions lead to quite different assemblies with potential implications for biomaterials design.





considerations become particularly acute as structural analyses of amyloidogenic peptide assemblies¹⁶ have demonstrated that polymorphism is often observed and depends critically on the assembly conditions.^{17–21}

In order to understand the structural principles that underlie the design of synthetic β sheet assemblies, we focused on an analysis of the self-complementary, amphipathic octapeptide sequence, Ac-FKFEFKFE-NH₂ (KFE8).^{22,23} The peptide design was based on an electrostatically self-complementary amphipathic sequence that was proposed to favor formation of antiparallel β sheets. Facile self-assembly occurred in aqueous solution, which resulted in formation of filamentous structures. A structural model was proposed for the KFE8 assemblies in which two cross- β filaments self-associate into left-handed helical ribbons. Atomic force microscopy (AFM) measurements confirmed the helical hand of the KFE8 assemblies.²² However, this model was insufficient to rationalize the observed curvature of the ribbon since it was based on symmetric face-to-face packing of antiparallel β sheet. Assemblies of KFE8 and related amphipathic β sheet sequences have been employed as synthetic biomaterials in tissue engineering and immunotherapy. ^{24,25} For these applications, detailed knowledge of the molecular structure of the assemblies is a critical consideration for the development of effective strategies to control interactions at the cell-biomaterial interface. We report here the cryoelectron microscopy (cryo-EM) structural analysis of KFE8 assembled under two different sets of conditions and identify the presence not only of helical ribbons but also of different populations of helical nanotubes.

This investigation provides evidence that supports the chaotic nature of peptide self-assembly and illustrates its potential impact on the corresponding structure of the assemblies. Computational/theoretical approaches have described the process of protein folding as an example of deterministic chaos; that is, as a currently unpredictable dynamical process in which the pathway varies as a consequence of small changes in initial conditions.^{26–28} If this hypothesis were valid for the folding processes that guide peptide self-assembly, it implies that final structures of the assemblies would be difficult to anticipate, even though these follow deterministically from the initial conditions (sequences, buffers, temperature, etc.). Peptide-based assemblies have been proposed as designer biomaterials, in which control of sequence affords more reliable control of structure and function. 1-3 However, recent high-resolution structural analyses of peptide and protein filaments have demonstrated that reliable prediction of supramolecular structure from sequence information remains a significant challenge to de novo design efforts.^{29–34} In addition, our results indicate that preparative conditions exert a significant influence on supramolecular structure and can direct the self-assembly process down different folding landscapes that can potentially affect the functional properties of the corresponding assemblies.

RESULTS

Different morphology of KFE8 nanotubes under cryo-EM

To determine the atomic structure of KFE8 assemblies, we imaged the peptide samples under two different conditions: the "ambient" sample was incubated at room temperature, while the "annealed" sample was heated to 90°C and slowly cooled to 25°C. The peptide was assembled under acidic conditions (10 mM sodium acetate buffer, pH 4.0), which had previously been demonstrated to slow down the assembly process and prevent irreversible aggregation of the assemblies. ^{22,23,35–37} In the ambient sample, consistent with other reports, ^{22,35} abundant ribbon-like filaments were seen after 18 h of incubation (Figures S1–S3). With longer incubations, the

¹Department of Biochemistry and Molecular Genetics, University of Virginia, Charlottesville, VA 22908, USA

²Department of Chemistry, Emory University, Atlanta, GA 30322, USA

³X-ray Science Division, Argonne National Laboratory, Lemont, IL 60439, USA

⁴The Robert P. Apkarian Integrated Electron Microscopy Core (IEMC), Emory University, Atlanta, GA 30322, USA

⁵Lead contact

^{*}Correspondence: egelman@virginia.edu (E.H.E.), vcontic@emory.edu (V.P.C.)

https://doi.org/10.1016/j.matt.2021.06.037

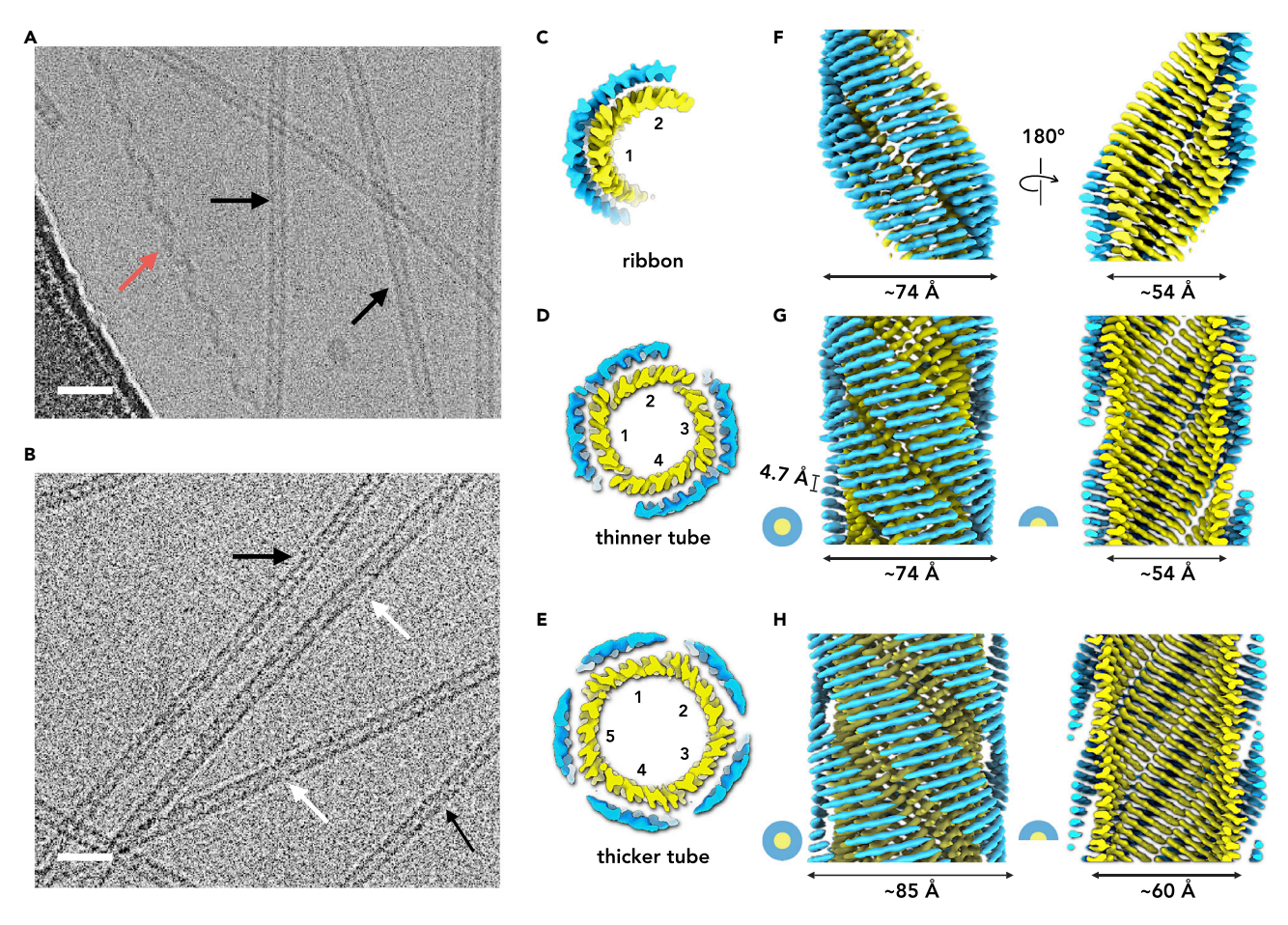


Figure 1. Cryo-EM of KFE8

(A) Cryoelectron micrograph of the KFE8 tubes assembled at ambient temperature. Scale bar, 20 nm. Black arrow points to the thinner tube and red arrow points to the ribbon.

(B) Cryoelectron micrograph of the annealed KFE8 tubes. The peptide was heated immediately after solubilization to 95°C and slowly cooled to 25°C. Scale bar, 20 nm. Black arrows point to the thinner tubes and white arrows point to the thicker tubes.

(C-E) Top view of the ribbon, thinner tube and thicker tube.

(F–H) Side views of the 3D reconstructions of the ribbon (F), thinner tube (G), and the thicker tube (H). The outer surface is shown on the left for each of these, while a cutaway view revealing the surface of the lumen is shown on the right.

ribbons gradually disappeared, and the presence of nanotubes was observed. After 2 weeks, cryo-EM imaging indicated that $\sim\!98\%$ of the filaments were nanotubes 7.5 nm in diameter and $\sim\!2\%$ were ribbons (Figure 1A). In the annealed sample, initial cryo-EM imaging indicated a stable, mixed population of nanotubes in which $\sim\!30\%$ were 7.5 nm in diameter, as seen in the ambient sample, while $\sim\!70\%$ were 8.5 nm in diameter (Figure 1B). The corresponding morphological changes correlated with conformational transitions observed in the circular dichroism (CD) spectra (Figure S2).

Three-dimensional (3D) reconstruction from two-dimensional (2D) cryo-EM images has now reached the stage in structural biology where near-atomic resolution is almost routinely achieved. 38,39 As a result, cryo-EM has recently emerged as a powerful tool in understanding peptide nanotube architectures. 29–34,40 We have taken advantage of the helical symmetry in these tubes to greatly improve the signal-to-noise ratio by helical averaging. The cryo-EM reconstructions clearly show that both the thinner tube (7.5 nm) and the thicker tube (8.5 nm) are double-





walled structures (Figures 1C–1E) in which thinner and thicker tubes consist of four and five cross- β sheet sandwiches, respectively. The ribbon, having two cross- β sheet sandwiches, is identical to half of the thinner tube (Figures 1C–1H and S4). In all structures, the KFE8 peptides pack tightly in the inner wall, with 4-fold and 5-fold rotational point-group symmetry in the thinner and thicker tubes, respectively. Interestingly, the four outer sheets in the thinner tube dimerize into two protofilaments, such that the 4-fold symmetry is broken in the outer wall (Figure 1D). As discussed below, the 2-fold symmetry can be broken further through a registry shift between protofilaments. In contrast to the inner wall, the outer sheets in the thicker tube do not make contact with each other (Figure 1H).

The doubled-wall nanotubes are made of both parallel and antiparallel sheets

Initial reconstructions of the thinner tube volume showed well-defined amino acid side chains and the typical zigzag pattern for the C α trace expected in a β strand. In contrast, such patterns were not seen in the outer wall (Figure S5). Based on the \sim 3.6-Å resolution map of the inner wall, and prior knowledge that this nanotube has a left-handed protofilament seen by AFM imaging, ^{22,23} we were able to build a reliable atomic model of parallel sheets in the inner wall, in contrast to the antiparallel arrangement that was previously predicted by molecular dynamics simulations. ^{22,23} Strikingly, when we tried to build parallel sheets into the outer wall, strong clashes existed between the carbonyl oxygen atoms such that the typical β sheet hydrogen bonds could not form (Figure S6). Therefore, we built antiparallel sheets into the outer wall, which resulted in the absence of clashes and formation of reasonable inter-strand hydrogen bonds.

To validate this hypothesis of inner parallel and outer antiparallel sheets, a single protofilament refinement was performed for the thinner tube (Figure 2A). The reconstruction (PDB: 7LQE) reached high resolution for both the inner and outer wall, and clearly revealed both an inner parallel sheet and an outer antiparallel sheet (Figures 2A and 2B). We were able to reconstruct a nearly identical structural arrangement for isolated, non-interacting ribbons (PDB: 7LQF) from an independent cryo-EM analysis of the corresponding filaments (Figures 1A and S4). The asymmetric unit (ASU) of the thinner tube and the ribbon consists of eight β strands: four inner strands in two parallel sheets and four outer strands in two antiparallel sheets (Figure 2B). The phenylalanine residues create a hydrophobic interface that stabilizes the interaction between the inner and outer walls. In contrast, hydrophilic residues line the inner lumen and cover the outer surface (Figure 2B). We used prior knowledge about the structure of the ribbon to determine that the thinner tube exists in two states in which the two ribbons are related by either a C₂ symmetry or a 2₁-like screw symmetry (Figure 2C). In the C₂ symmetry (PDB: 7LQG), the two protofilaments are in register. In the screw symmetry (PDB: 7LQH), they are shifted by a strand, such that the polarity of the strands is reversed through rotation of one protofilament into the other. While no contacts are observed between the two protofilaments in the outer wall, the contacts between protofilaments in the inner wall are only made via a few hydrogen bonds (Figure 2D). Despite the unpredicted antiparallel-on-parallel packing of β sheets at the outer-inner interface, structural homology searches of the PDB indicated that this arrangement occurred at a similar frequency within native protein structures when accounting for the statistical preference for antiparallel versus parallel sheet (Figure S7).42

Similar results were observed in the structural analysis of the thicker tube. The structure of the inner wall was determined at high resolution (\sim 3.6 Å) and found to be based on parallel β sheets (PDB: 7LQI). Due to difficulties in signal subtraction and





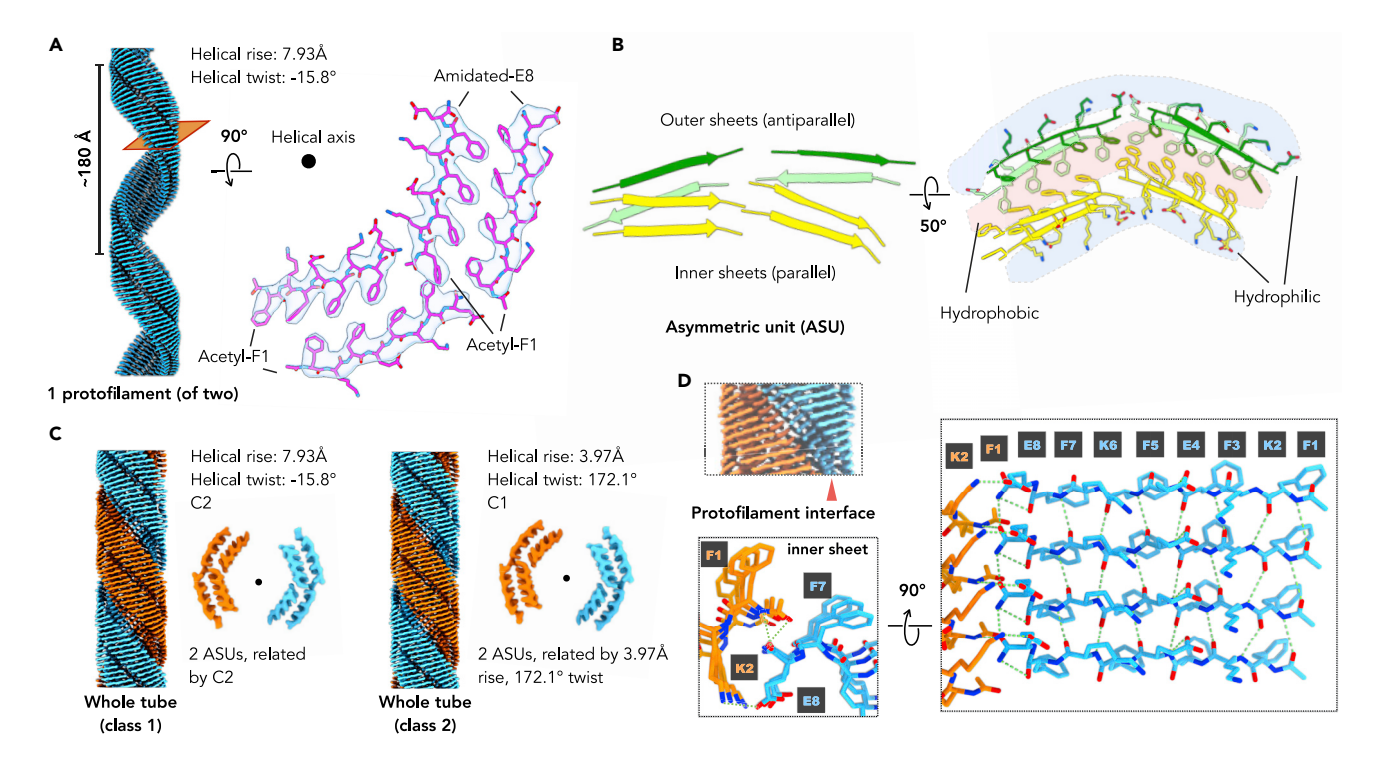


Figure 2. The thinner tube is made of two ribbons

- (A) The cryo-EM structure of one of two protofilaments that form the thinner tube. The surface of this protofilament from the helical reconstruction is on the left. The high-resolution cross-sectional density map is on the right, with the atomic model built into the map shown.
- (B) The ASU of the thinner tube contains eight strands: the parallel inner strands are in yellow, while the antiparallel outer strands are in green and light green. The hydrophobic interactions within the ASU involve the interdigitated phenylalanine residues.
- (C) The thinner tubes can be sorted into two classes, in which the two protofilaments are related by either a C_2 symmetry (class 1) or a screw symmetry (class 2).
- (D) The protofilament interface exists in the inner wall only. The hydrogen bonds are highlighted between protofilaments and within parallel sheets.

the absence of corresponding ribbon filaments, we could not obtain a high-resolution structure for the outer wall (Figure 3A). However, using a similar analysis of steric clash as employed for the thinner tube, we could demonstrate that parallel sheets are impossible for the outer wall (Figure S6). The ASU in the thicker tube consists of four strands: two in the inner parallel sheet and two in the outer antiparallel sheet, with similar interfaces seen in the thinner tube (Figure 3B). As with the thinner tubes, the contacts between protofilaments are mediated exclusively through hydrogen-bonding interactions between strands in the inner wall (Figure 3C). The observed differences in assembly structures under different preparative conditions were representative of the respective population differences. The observed synchrotron small-angle X-ray scattering (SAXS) intensity profiles for the ambient and annealed samples could be simulated effectively using all-atom models derived from the cryo-EM structures of the thinner (PDB: 7LQG) and thicker nanotubes (PDB: 7LQI), respectively (Figure S8).

Different helical packing from the same 8-residue peptide

A structural comparison of the thinner and thicker tubes revealed subtle differences in protomer packing arrangements. The tilt angle of the peptides in the thinner tube, defined with respect to the plane normal to the filament axis, was observed to be 31° and 14° for the inner and outer sheets, respectively. The corresponding tilt angles in the thicker tube are 30° and 13° . The difference in tilt angle between the inner and





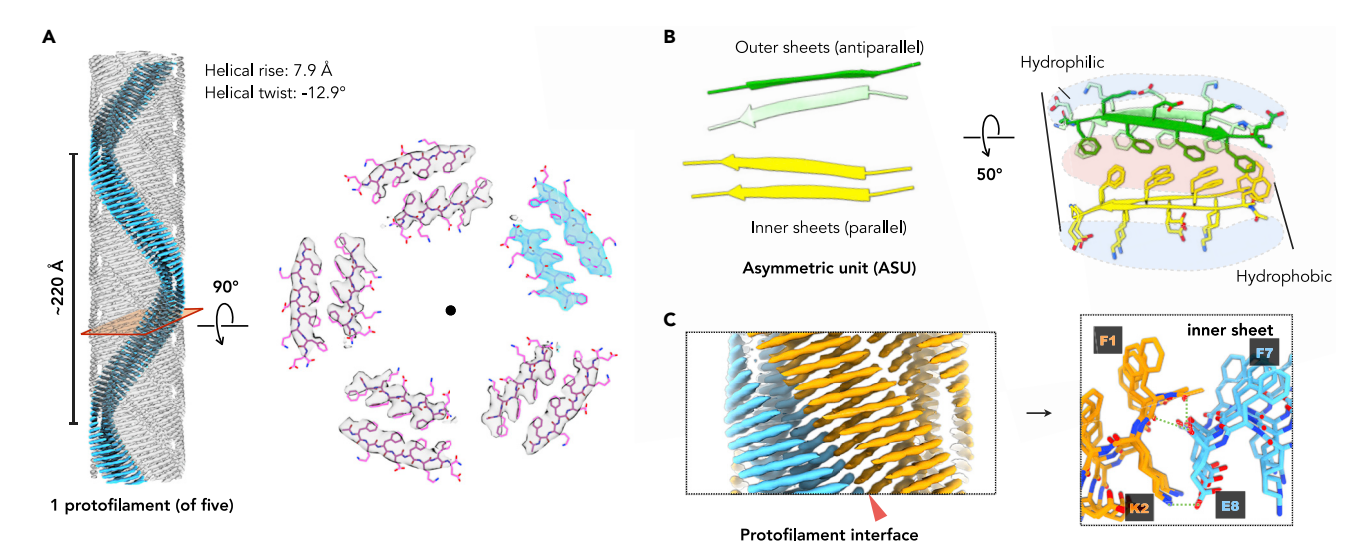


Figure 3. The thicker tube forms after annealing

- (A) The thicker tube cryo-EM structure. The 5-fold averaged helical reconstruction is on the left, with a single protofilament shown in cyan. The cross-sectional density map is on the right, with an atomic model built into the map.
- (B) The ASU of the thicker tube. The hydrophobic interactions within the ASU arise from the interdigitated phenylalanine residues.
- (C) The protofilament interface exists only in the inner wall. The hydrogen bonds between protofilaments are shown as dotted lines.

outer sheet was conserved at 17° for both tubes (Figure 4A). A structural comparison of two β strand peptides in the inner wall indicated that the packing arrangement was nearly identical between the thinner and the thicker tubes (root-mean-square deviation [RMSD] of only 0.2 Å). However, when comparing 10 peptide strands, the RMSD increases 4.5 times to 0.9 Å, which arises from a slight difference in twist angle between the adjacent strands in the parallel β sheet between the thinner (-7.9° per strand) and thicker (-6.4° per strand) tubes (Figure 4B).

Next, we investigated the protofilament interfaces between the two inner sheets. The hydrogen bonds are quite similar between the thinner and thicker tubes (Figures 2D and 3C). When we aligned one sheet of the two, we observed a \sim 7° rotation in the other sheet. As with the difference in twist within the inner sheets (-7.9°) vs -6.4° per strand), this shows that the protofilament interface has a plasticity for such contacts. A similar phenomenon has been reported in our recent study of α -helical peptide assemblies. 34 The difference in β sheet orientation for the inner (parallel) and outer (antiparallel) walls of the nanotubes leads to different interfacial packing arrangements between the inner and outer β sheets. As a consequence of the larger ASU, the thinner tube displays four distinct interfacial arrangements; two interfaces for each half-protofilament. In contrast, the thicker tube consists of only two interfaces, which are common to the five protofilaments. This pair of interfaces in the thicker tube is structurally similar to the interfaces within one of the half-protofilaments of the thinner tube (Figures 4D and 4E). These interfaces comprise interdigitated phenylalanine residues, which are arranged similarly to the pairwise β-zipper packing of strands in amyloid fibers. 43,44

DISCUSSION

The KFE8 peptide was initially designed 22,23 to form a synthetic cross- β fibril assembly in which the alternating hydrophilic-hydrophobic sequence reinforced the dyad fiber repeat of a β sheet. Polar sequence patterning has been employed frequently as a design principle to bias peptide conformation and direct protein





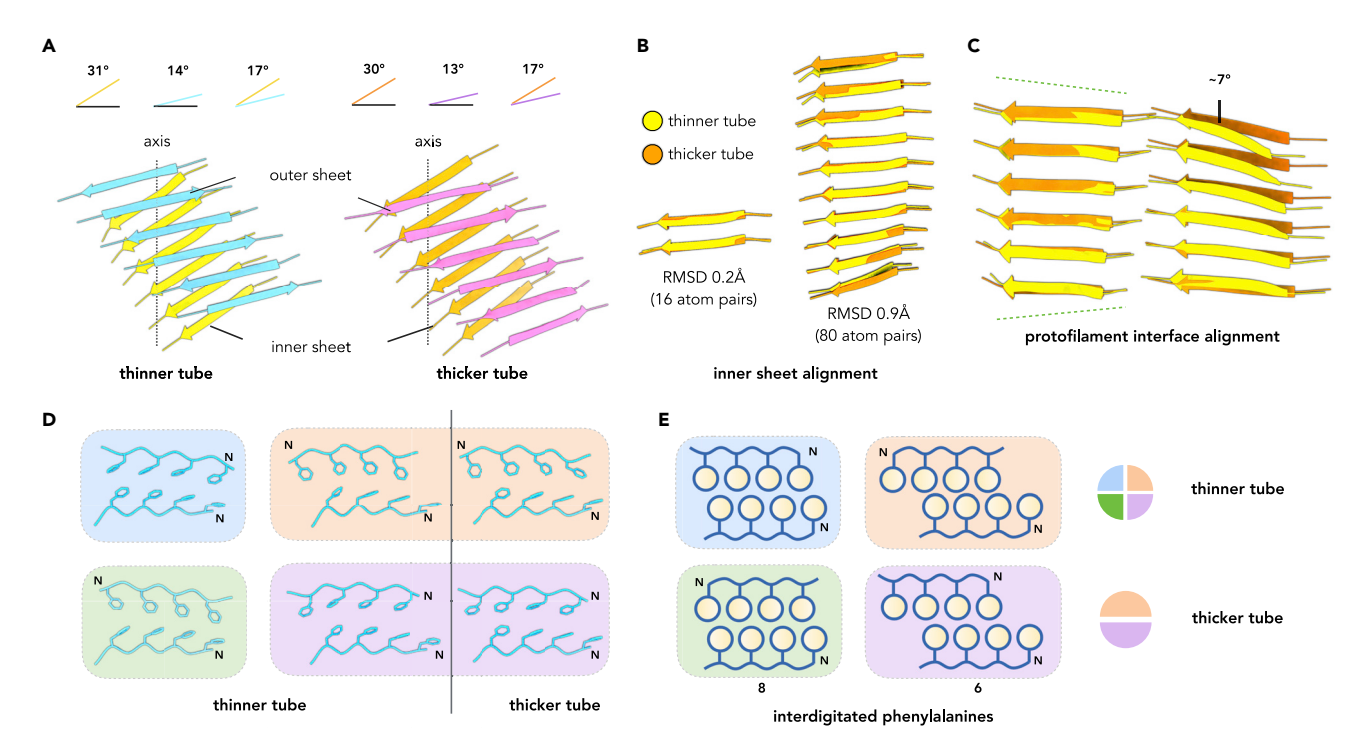


Figure 4. The different helical packings of the same eight-residue peptide

- (A) One stack containing one sheet of the inner wall and one sheet of the outer wall (thinner tube on the left and thicker tube on the right). The tilt angles of the sheet from the plane normal to the helical axis are indicated on top.
- (B) Structural alignment of a single inner β sheet containing 2 strands (left) and 10 strands (right).
- (C) Structural comparison of two adjacent inner β sheets containing six strands. The alignment was made on the left sheets, resulting in the twist differences on the right.

(D and E) The inner-outer strand pairs in the thinner and thicker tube. A cartoon illustration is shown in (E). The N terminus of the peptide is labeled. Structurally similar interfaces within the thinner and thicker tubes are highlighted in the same color. The ASU of protofilaments within the thicker tube have the same pairwise arrangement of interfaces (magenta and orange) under the imposed helical symmetry as one pair of interfaces within the thinner tube. The ASU of the protofilaments within the thinner tubes shows an additional pair of interfacial interactions (blue and green).

self-association. 45-48 In KFE8, the pattern of polar, charged residues was chosen to reinforce an antiparallel orientation through introduction of a network of complementary electrostatic interactions between adjacent β strands within the presumed cross-β filament that would arise from peptide self-assembly. ^{22,23} Structural analyses of β sheets in native proteins indicated a preference for the antiparallel orientation, ⁴⁹ particularly for sequences that comprise alternating patterns of polar and non-polar residues. 50 Interestingly, it was observed some time ago that antiparallel sheets tend to be found on the outside of proteins and parallel ones in the interior, and this was attributed to the greater conformational flexibility of the antiparallel sheet. 51 In both the thinner and thicker tubes, the antiparallel sheets are located on the outside, while the inner layer of the tube consists solely of parallel β sheet. In the latter case, close contact occurs between parallel strands in the inner sheet despite the fact that the cross strand electrostatic interactions should be repulsive in nature. However, the respective polar surfaces of the bilayer sheets should be highly hydrated within the protofilaments and nanotubes, which may screen repulsive interactions between polar sidechains in the parallel sheet. In addition, both attractive and repulsive charge-charge interactions would be attenuated at acidic pH due to partial protonation of the glutamic acid sidechains. Therefore, electrostatic interactions may not play a determinative role in selection of strand orientation. Theoretically high surface charge densities do not necessarily abrogate self-assembly in solution, as





has been demonstrated for nanotube formation from surfactant-like synthetic peptide sequences. 52-59

While it has been known that the sequence of a peptide or protein will influence whether a parallel or antiparallel β sheet is formed, 49,50,60 the same KFE8 peptide sequence readily forms both parallel sheets and antiparallel sheets within the same protofilaments (Figures 2 and 3). Statistical analyses of the PDB (Figure S9) indicate that the antiparallel-on-parallel sheet packing within the protofilament has clear precedent among native protein structures, but the preference for this mode of sheet lamination, vis-à-vis either the parallel-parallel or antiparallel-antiparallel packing arrangements, remains unclear at this point. However, this packing arrangement does account for the helical curvature of the bilayer ribbons, which has been reproducibly observed in the literature for KFE8 assemblies. 22,23,35

Our results demonstrate that plasticity in the structure of the β sheets formed by the KFE8 peptide, and plasticity in the interfaces between these sheets, leads to polymorphism in the assembly of ribbons and nanotubes formed by this peptide. A plasticity in the packing of proteins was invoked many years ago in the theory of quasi-equivalence to explain how identical copies of proteins might be situated in non-identical environments to form icosahedral viral capsids.⁶¹ This plasticity can be seen in the polymerization of tubulin in vitro, where microtubules are formed with between 8 and 17 protofilaments, while in vivo this number is almost always 13.62 Similarly, amyloidogenic peptides have been demonstrated to polymerize into structurally distinct filaments when assembled in vitro versus in vivo. 19-21 In addition, the amyloidogenic oligopeptide sequence $A\beta(16-22)^{63}$ has been observed to assemble in vitro into either nanotubes or ribbons in a manner that depends solely on peptide concentration. ⁶⁴ Therefore, even subtle variations in assembly conditions may result in significant differences in supramolecular structure that can have consequences for functional applications. The differences in self-assembly behavior that have been observed for β sheet peptide filaments have been interpreted in terms of analytical models based on the free energies of the respective assemblies. 10,65,66 However, our results imply that we do not fully understand at present the structural complexity of the folding landscape even for assemblies based on relatively simple peptide sequences.

We suggest that the structural plasticity observed in the self-assembly of KFE8 and other designed peptides can be understood as a manifestation of deterministic chaos in the self-assembly process. Protein dynamics ^{67,68} and protein folding ^{26–28} have been described as chaotic processes, in which the trajectories are probabilistic and strongly influenced by small differences in initial conditions. Despite its chaotic nature, the folding process is not incommensurate with convergence on a unique native conformation as embodied in the folding funnel concept. Even though the folding pathway may not be predictable, it does not diverge to infinity and remains confined within a diverse but limited conformational space. In addition, this situation does not preclude the fact that structural correlations can be defined in three dimensions for the native conformation of stable, folded proteins. The recent stunning success in the application of knowledge-based algorithms in protein structural prediction implies that such correlations can be effectively employed in a predictive manner from sequence information. ^{69,70}

In contrast, KFE8, as a designed peptide, does not necessarily converge to a unique native structure. Similar behavior has been observed for many other peptides that form β sheet assemblies, particularly amyloidogenic sequences. In the latter case, disparate morphologies are observed that depend strongly on assembly conditions,





either in vivo or in vitro. KFE8 and many other designed, synthetic, self-assembling peptides are characterized by limited complexity sequences and low information volume. These peptides may be compared with intrinsically disordered proteins (IDPs), which display similar sequence features (i.e., low complexity and information content). The dynamic conformational behavior of the latter systems never converges to a native conformation, 71 and has been interpreted in terms of the mathematics of deterministic chaotic systems.⁷² While the dynamic behavior associated with the folding/self-assembly of KFE8 may be interpreted as chaotic, our results indicate that the peptide can converge to different structures through self-assembly under different initial conditions. As previous structure analyses of natural and designed peptides have revealed, ^{17-21,29,31-34} the chaotic nature of the self-assembly process precludes prediction of the folding trajectory. Moreover, the structural complexity of the resultant assemblies and limited database of high-resolution structures are significant obstacles at present to the application of knowledge-based approaches to reliable structural prediction. In addition, the inherent limitations in sequence complexity observed for simple oligopeptide systems such as KFE8, which are often employed as substrates in materials applications, may necessarily result in structural polymorphism in the resultant assemblies.

Conclusion

We demonstrate that the self-assembly of KFE8 results in the formation of ribbons and nanotubes that differ in structure when assembled under different conditions. We propose that this process represents an instance of deterministic chaos, in which small differences in nucleation and folding events lead to quite different assemblies being formed. While the process of self-assembly is deterministic (as opposed to something that is truly stochastic, such as quantum uncertainty), this does not imply that the process is predictable at the current time given the limitations of our knowledge and tools. What are the implications of this statement for the design of peptide assemblies? Clearly, computational and theoretical approaches to understand peptide assemblies²³ are unable at this point to yield correct structures due to the complexity of the problem, inadequate force fields, and limited computational power. Since these assemblies obey deterministic laws of chemistry and physics, we do not suggest that this will always be the case. Experimental techniques, especially cryo-EM, will have an extremely important role to play until we can be in a position to accurately simulate and reliably predict the structures of such assemblies *in silico*.

Peptide assemblies, such as those derived from KFE8, are being actively investigated as medical biomaterials. Our results suggest that the structures of these assemblies depend critically on preparative conditions. Structural variations in the assemblies may affect interactions at the cell-biomaterial interface in a manner that is difficult to predict but is crucial for success in biomedical applications. In addition, as has previously been demonstrated for other peptide assemblies, ^{29,34} sequence-structure correlations derived from the analysis of soluble, globular proteins may provide limited predictive insight into the reliable design of filamentous peptide nanomaterials. Therefore, high-resolution structural analyses of native and synthetic assemblies are essential to build databases that can be employed as a resource of information to guide reliable structural prediction and sequence design of self-assembling peptides.

EXPERIMENTAL PROCEDURES

Resource availability

Lead contact

Further information and requests for resources and reagents should be directed to, and will be fulfilled by, the lead contact, Vincent P. Conticello (vcontic@emory.edu).





Materials availability

This study did not generate previously unreported reagents.

Data and code availability

Reconstruction maps were deposited in the Electron Microscopy Data Bank with accession numbers of EMD-23483, EMD-23484, EMD-23485, EMD-23486, and EMD-23487. The corresponding filament models were deposited in the PDB with accession numbers of PDB: 7LQE, PDB: 7LQF, PDB: 7LQG, PDB: 7LQH, and PDB: 7LQI. Additional data that support the findings of this study are available from the corresponding authors upon request. The code for MASTER is freely available for noncommercial purposes from the Grigoryan Lab at Dartmouth College through the following link: https://grigoryanlab.org/master.

Peptide synthesis and assembly

KFE8 peptide, Ac-FKFEFKFE-NH2, was obtained from GenScript USA Inc (Piscataway, NJ) as the N-acetyl, C-amide derivative at \geq 95% purity by analytical HPLC. Stock solutions of the KFE8 peptide (3 mg·mL $^{-1}$) were prepared by solubilizing 0.75 mg of purified, lyophilized peptide in 250 μ L of sodium acetate buffer (10 mM, pH 4.0) via sonication for 4–5 min. 35 The solutions were allowed to either incubate at ambient temperature or were subjected to the following annealing protocol in a thermal cycler: (1) rapid heating to 90°C for 30 min and (2) cooling to 25°C at a rate of 0.2°C/min. The ambient sample consisted primarily of ribbons at short incubation times (\leq 18 h). The population of nanotubes slowly increased upon incubation at ambient temperature, eventually becoming the major population over a period of 2 weeks. Few ribbons were observed in the annealed sample, and the population of nanotubes did not appear to change upon extended incubation at ambient temperature.

CD spectropolarimetry

CD measurements were performed on a Jasco J-1500 CD spectropolarimeter using 0.20-mm thick quartz plates from Hellma USA Inc (Plainview, NY). Three spectra were collected and averaged in a wavelength range from 190 to 260 nm at a scanning range of 100 nm/min with a bandwidth of 2 nm and a data pitch of 0.2 nm.

Negative stain transmission electron microscopy analysis

Grids were prepared using diluted solutions of peptide (3 $mg \cdot mL^{-1}$) in aqueous buffer (10 mM acetate, pH 4.0). Samples were prepared by depositing 4 μL of peptide solution onto a 200-mesh carbon-coated copper grid from Electron Microscopy Services (Hatfield, PA). After 90 s of incubation on the grid, moisture was wicked away, leaving a thin film of sample. An aliquot (4 μL) of negative stain solution (1% uranyl acetate) was deposited onto the thin film. After 60 s of staining, the remaining moisture was wicked away, and the grid dried in a tabletop desiccator *in vacuo* for at least 5 min. Electron micrographs were recorded on a Hitachi HT-7700 transmission electron microscope with a tungsten filament and Advanced Microscopy Techniques charge-couupled device (CCD) camera at an accelerating voltage of 80 kV.

Motif analysis

A search database was created by filtering the PDB, as of 9 December, 2020, using the following criteria: X-ray structures with resolution of 2.6 Å or better with no more than 5,000 residues and no more than 26 chains in the biological unit. This search resulted in a total of 185,302 biological-unit entries. This set of structures was employed as the database in structural homology searchers using computational algorithm MASTER. 73,74 A minimal assembly motif was constructed from four β strands





(two inner plus two outer) derived from a cross-β interface from the single protofilament reconstruction of the thinner tube (PDB: 7LQE). In order to eliminate artifacts due to the peptide termini, the N-terminal Phe and C-terminal Glu residues of KFE8 were trimmed in PyMol to generate a query structure (KFEFKF) that consisted of four β strands, each of six residues. Two structural variants of KFEFKF were generated in which the orientations of inner and outer strands were changed to antiparallel and parallel respectively. The respective structures comprise antiparallel/antiparallel and parallel/parallel interfaces, which were employed as control motifs in structural homology searches. These controls generated by aligning the strands with the desired orientation to the strands with the undesired orientation in PyMol. The three motifs (KFEFKF and two controls) were employed as query structures in MASTER searches of the compiled database. All unique and non-redundant matches (i.e., less than 50% sequence identity compared with the queried sequence) with full-backbone RMSD below 2.0 Å were sought and used in the subsequent analysis.

Synchrotron SAXS/wide-angle X-ray scattering measurements

Synchrotron SAXS/wide-angle X-ray scattering (WAXS) measurements were performed at the 12-ID-B beamline of the Advanced Photon Source at Argonne National Laboratory. A SAXS/WAXS simultaneous setup was utilized, and the sample-to-detector distances were set such that the overall scattering momentum transfer (q) range was achieved from 0.003 to 2.4 Å⁻¹, where $q = 4\pi \sin(\theta)/\lambda$, with 2θ denoting the scattering angle and λ denoting the X-ray wavelength. The wavelength was set at 0.9322 Å during the measurements. Scattered X-ray intensities were measured using a Pilatus 2 M (DECTRIS) detector for SAXS and Pilatus 300K for WAXS. SAXS/WAXS measurements were performed on aqueous solutions of the annealed and ambient KFE8 peptide assemblies at concentrations of 4.0 mg/mL (circa 3.4 mM) in acetate buffer (10 mM, pH 4.0) at 25°C. Prior to SAXS analysis, the peptide solutions were dialyzed against a large excess of pure buffer for 24 h. A flow cell equipped with a quartz capillary (1.5-mm diameter) was used to prevent radiation damage. Twenty images were collected for each sample and buffer. The 2D scattering images were converted to 1D SAXS curves through azimuthally averaging after solid angle correction and then normalizing with the intensity of the transmitted X-ray beam using the software package at beamline 12-ID-B. The 1D curves of the samples were averaged and subtracted with the background measured from the corresponding buffers. The simulated SAXS curves were calculated using the program CRYSOL⁷⁵ with fitting to all-atom cryo-EM structural models. To reproduce the SAXS features, the length of the model was made about 10 times the diameter.

Cryo-EM imaging and analysis

The peptide sample (\sim 2–2.5 μ L) was applied to glow-discharged lacey carbon grids, and then plunge frozen using an EM GP Plunge Freezer (Leica). The cryo-EMs were collected on a 300-keV Titan Krios with a K3 camera (University of Virginia) at 1.08 Å/pixel and a total dose of \sim 50 e/Ų. The micrographs were first motion corrected and dose weighted by MotionCorr v2, ⁷⁶ and then contrast transfer function (CTF) correction was applied by multiplying the images with the theoretical CTF. Filament images corresponding to \sim 20 electrons/Ų were extracted using EMAN2. ⁷⁷ For each peptide filament, a list of possible helical symmetries was calculated from the averaged power spectrum of peptide particles (Figures S5 and S8). To determine the correct helical symmetry from the list, first, if the full dataset has more than 30,000 particles, a subset containing 30,000 particles was generated. Then the initial volume was generated from those 30,000 particles with random assigned azimuthal angles. After that, possible helical symmetries were tested in Spider using





iterative helical real space reconstruction (IHRSR)^{78,79} by trial and error until recognizable amino acid side chain densities could be observed in the correct symmetry. Specifically, the IHRSR reconstructions were divided into three steps, where 4× binned, 2× binned, and finally un-binned particles were used to accelerate the progress. Helical symmetries were tightly locked in the first two steps, and then slightly relaxed in the third step. All helical parameters, including rise, rotation, and point-group symmetry, were imposed at the end of each IHRSR cycle. Since the KFE8 nanotubes are made of only β sheets, the helical hand cannot be easily determined from the cryo-EM volume directly, unlike volumes that contain an α helix, in which the hand is obvious when the resolution is 4.5 Å or better. Therefore, the hand was determined using prior knowledge of previously reported AFM results, where left-handed ribbons were reported. 22,23

Additional refinement of 1-protofilament

A detailed workflow for the cryo-EM analysis of the thinner tube is shown in Figure S5. After determining the correct symmetry for the inner wall, a reconstruction using all particles was run in Spider. The resulting volumes were then imported into RELION for a 3D classification. Interactive 3D classifications were run in RELION for a potential separation of the two classes (T = 4 to T = 200), but the outcome was not ideal. Therefore, we used RELION particle subtraction to generate an image stack containing the signal of 1-protofilament and exported the stack back to Spider for IHRSR. This ended up with a \sim 3.4-Å resolution reconstruction for the 1-protofilament of the thinner tube (Figure S10). C2 and 2₁-like references were generated from the 1-protofilament volume and these models were used for reference-based sorting. All maps were filtered to 3.0 Å without B factor in Spider and then used as input in a newly developed map sharpening tool, DeepEMhacer. This sharpening result is slightly better than maps sharpened with a negative B factor. The statistics are listed in Table S1.

Model building

The eight-residue KFE8 model was generated in Chimera ⁸² from the corresponding peptide sequence and then docked in the electron microscopy maps. The ASU model was adjusted manually in Coot ⁸³ to best fit into the map. Then, this adjusted ASU model was used to generate a model filament using the determined helical symmetry, which was then refined against the full cryo-EM map using real-space refinement in PHENIX. ⁸³ The refinement statistics are shown in Table S1. Cryo-EM maps and atomic coordinates have been deposited with the Electron Microscopy Data Bank and PDB with accession codes given in Table S1. Model versus map Fourier shell correlation (FSC) calculations were employed to estimate the resolution of the reconstructions and are reported in Figure S10. Map-map FSC calculations are reported in Figure S11.

SUPPLEMENTAL INFORMATION

Supplemental information can be found online at https://doi.org/10.1016/j.matt. 2021.06.037.

ACKNOWLEDGMENTS

Cryo-EM imaging was conducted at the Molecular Electron Microscopy Core facility at the University of Virginia, which is supported by the School of Medicine and built with National Institutes of Health (NIH) grant G20-RR31199. In addition, the Titan Krios (SIG S10-RR025067) and K3/GIF (U24-GM116790) were purchased, in part or in full, with the designated NIH grants. This study was supported by the

Matter Article



Robert P. Apkarian Integrated Electron Microscopy Core (IEMC) at Emory University, which is subsidized by the School of Medicine and Emory College of Arts and Sciences. Negative stain TEM images were acquired on a Hitachi HT7700 120kV TEM at Emory University, which was supported by the Georgia Clinical and Translational Science Alliance under award number UL1TR002378. The content is solely the responsibility of the authors and does not necessarily reflect the official views of the NIH. This research was supported by grants from the National Science Foundation (NSF) (DMR-1534317) to V.P.C., the NIH (GM138756) to F.W., and the NIH (GM122510) to E.H.E. The circular dichroism spectropolarimeter was acquired through funding from an NSF grant (DBI-1726544). This research used resources of the Advanced Photon Source, a US Department of Energy (DOE) Office of Science User Facility, operated for the DOE Office of Science by Argonne National Laboratory under contract no. DE-AC02-06CH11357. The authors thank Dr. Gevorg Grigoryan for useful discussions.

AUTHOR CONTRIBUTIONS

Conceptualization, F.W., O.G., E.H.E., and V.P.C.; methodology, F.W., E.H.E., and V.P.C.; investigation, F.W., O.G., S.W., T.O., and X.Z.; supervision, E.H.E. and V.P.C.; validation, F.W. and E.H.E.; visualization, F.W., E.H.E., and V.P.C.; writing – original draft, F.W., E.H.E., and V.P.C.; writing – review and editing, F.W., E.H.E., and V.P.C.; funding acquisition, F.W., E.H.E., and V.P.C.

DECLARATION OF INTERESTS

The authors declare no competing interests.

Received: April 1, 2021 Revised: May 26, 2021 Accepted: June 21, 2021 Published: July 27, 2021

REFERENCES

- Bowerman, C.J., and Nilsson, B.L. (2012). Review self-assembly of amphipathic β-sheet peptides: insights and applications. Pept. Sci. 98, 169–184.
- Zhang, S. (2017). Discovery and design of selfassembling peptides. Interf. Focus 7, 20170028.
- Beesley, J.L., and Woolfson, D.N. (2019). The de novo design of α-helical peptides for supramolecular self-assembly. Curr. Opin. Biotechnol. 58, 175–182.
- Zhang, S., Holmes, T., Lockshin, C., and Rich, A. (1993). Spontaneous assembly of a selfcomplementary oligopeptide to form a stable macroscopic membrane. Proc. Natl. Acad. Sci. U S A 90, 3334–3338.
- Aggeli, A., Bell, M., Boden, N., Keen, J.N., Knowles, P.F., McLeish, T.C.B., Pitkeathly, M., and Radford, S.E. (1997). Responsive gels formed by the spontaneous self-assembly of peptides into polymeric β-sheet tapes. Nature 386, 259–262.
- Schneider, J.P., Pochan, D.J., Ozbas, B., Rajagopal, K., Pakstis, L., and Kretsinger, J. (2002). Responsive hydrogels from the intramolecular folding and self-assembly of a

- designed peptide. J. Am. Chem. Soc. 124, 15030–15037.
- Eanes, E.D., and Glenner, G.G. (1968). X-ray diffraction studies on amyloid filaments. J. Histochem. Cytochem. 16, 673–677.
- Sunde, M., Serpell, L.C., Bartlam, M., Fraser, P.E., Pepys, M.B., and Blake, C.C. (1997). Common core structure of amyloid fibrils by synchrotron X-ray diffraction. J. Mol. Biol. 273, 779–739
- Diaz-Avalos, R., Long, C., Fontano, E., Balbirnie, M., Grothe, R., Eisenberg, D., and Caspar, D.L. (2003). Cross-beta order and diversity in nanocrystals of an amyloid-forming peptide. J. Mol. Biol. 330, 1165–1175.
- Aggeli, A., Nyrkova, I.A., Bell, M., Harding, R., Carrick, L., McLeish, T.C., Semenov, A.N., and Boden, N. (2001). Hierarchical self-assembly of chiral rod-like molecules as a model for peptide beta-sheet tapes, ribbons, fibrils, and fibers. Proc. Natl. Acad. Sci. U S A 98, 11857– 11862.
- Lee, M., Wang, T., Makhlynets, O.V., Wu, Y., Polizzi, N.F., Wu, H., Gosavi, P.M., Stohr, J., Korendovych, I.V., DeGrado, W.F., et al. (2017). Zinc-binding structure of a catalytic amyloid

- from solid-state NMR. Proc. Natl. Acad. Sci. U S A 114, 6191–6196.
- Nagy-Smith, K., Moore, E., Schneider, J., and Tycko, R. (2015). Molecular structure of monomorphic peptide fibrils within a kinetically trapped hydrogel network. Proc. Natl. Acad. Sci. U S A 112, 9816–9821.
- Cormier, A.R., Pang, X., Zimmerman, M.I., Zhou, H.X., and Paravastu, A.K. (2013). Molecular structure of RADA16-I designer selfassembling peptide nanofibers. ACS Nano 7, 7562–7572.
- Knowles, T.P., Fitzpatrick, A.W., Meehan, S., Mott, H.R., Vendruscolo, M., Dobson, C.M., and Welland, M.E. (2007). Role of intermolecular forces in defining material properties of protein nanofibrils. Science 318, 1900–1903.
- Schleeger, M., vandenAkker, C.C., Deckert-Gaudig, T., Deckert, V., Velikov, K.P., Koenderink, G., and Bonn, M. (2013). Amyloids: from molecular structure to mechanical properties. Polymer 54, 2473–2488.
- Ke, P.C., Zhou, R., Serpell, L.C., Riek, R., Knowles, T.P.J., Lashuel, H.A., Gazit, E., Hamley, I.W., Davis, T.P., Fändrich, M., et al.





- (2020). Half a century of amyloids: past, present and future. Chem. Soc. Rev. 49, 5473–5509.
- Close, W., Neumann, M., Schmidt, A., Hora, M., Annamalai, K., Schmidt, M., Reif, B., Schmidt, V., Grigorieff, N., and Fandrich, M. (2018). Physical basis of amyloid fibril polymorphism. Nat. Commun. 9, 699.
- Guenther, E.L., Ge, P., Trinh, H., Sawaya, M.R., Cascio, D., Boyer, D.R., Gonen, T., Zhou, Z.H., and Eisenberg, D.S. (2018). Atomic-level evidence for packing and positional amyloid polymorphism by segment from TDP-43 RRM2. Nat. Struct. Mol. Biol. 25, 311–319.
- Zhang, W., Falcon, B., Murzin, A.G., Fan, J., Crowther, R.A., Goedert, M., and Scheres, S.H. (2019). Heparin-induced tau filaments are polymorphic and differ from those in Alzheimer's and Pick's diseases. eLife 8, e43584.
- Kollmer, M., Close, W., Funk, L., Rasmussen, J., Bsoul, A., Schierhorn, A., Schmidt, M., Sigurdson, C.J., Jucker, M., and Fändrich, M. (2019). Cryo-EM structure and polymorphism of Aβ amyloid fibrils purified from Alzheimer's brain tissue. Nat. Commun. 10, 4760.
- Bansal, A., Schmidt, M., Rennegarbe, M., Haupt, C., Liberta, F., Stecher, S., Puscalau-Girtu, I., Biedermann, A., and Fändrich, M. (2021). AA amyloid fibrils from diseased tissue are structurally different from in vitro formed SAA fibrils. Nat. Commun. 12, 1013.
- 22. Marini, D.M., Hwang, W., Lauffenburger, D.A., Zhang, S., and Kamm, R.D. (2002). Left-handed helical ribbon intermediates in the self-assembly of a β-sheet peptide. Nano Lett. 2, 295–299.
- Hwang, W., Marini, D.M., Kamm, R.D., and Zhang, S. (2003). Supramolecular structure of helical ribbons self-assembled from a β-sheet peptide. J. Chem. Phys. 118, 389–397.
- Rudra, J.S., Sun, T., Bird, K.C., Daniels, M.D., Gasiorowski, J.Z., Chong, A.S., and Collier, J.H. (2012). Modulating adaptive immune responses to peptide self-assemblies. ACS Nano 6, 1557–1564.
- Wan, S., Borland, S., Richardson, S.M., Merry, C.L.R., Saiani, A., and Gough, J.E. (2016). Selfassembling peptide hydrogel for intervertebral disc tissue engineering. Acta Biomater. 46, 29–40.
- Böhm, G. (1991). Protein folding and deterministic chaos: limits of protein folding simulations and calculations. Chaos Solitons Fractals 1, 375–382.
- Bahi, J.M., Côté, N., and Guyeux, C. (2011). Chaos of protein folding. In The 2011 International Joint Conference on Neural Networks, pp. 1948–1954.
- Bahi, J.M., Côté, N., Guyeux, C., and Salomon, M. (2012). Protein folding in the 2D hydrophobic-hydrophilic (HP) square lattice model is chaotic. Cognit Comput. 4, 98–114.
- Egelman, E.H., Xu, C., DiMaio, F., Magnotti, E., Modlin, C., Yu, X., Wright, E., Baker, D., and Conticello, V.P. (2015). Structural plasticity of helical nanotubes based on coiled-coil assemblies. Structure 23, 280–289.

- DiMaio, F., Song, Y., Li, X., Brunner, M.J., Xu, C., Conticello, V., Egelman, E., Marlovits, T., Cheng, Y., and Baker, D. (2015). Atomicaccuracy models from 4.5-A cryo-electron microscopy data with density-guided iterative local refinement. Nat. Methods 12, 361–365.
- 31. Hughes, S.A., Wang, F., Wang, S., Kreutzberger, M.A.B., Osinski, T., Orlova, A., Wall, J.S., Zuo, X., Egelman, E.H., and Conticello, V.P. (2019). Ambidextrous helical nanotubes from self-assembly of designed helical hairpin motifs. Proc. Natl. Acad. Sci. U S A 116, 14456–14464.
- 32. Chen, Y.X., Ing, N.L., Wang, F., Xu, D., Sloan, N.B., Lam, N.T., Winter, D.L., Egelman, E.H., Hochbaum, A.I., Clark, D.S., et al. (2020). Structural determination of a filamentous chaperone to fabricate electronically conductive metalloprotein nanowires. ACS Nano 14, 6559–6569.
- Feng, Z., Wang, H., Wang, F., Oh, Y., Berciu, C., Cui, Q., Egelman, E.H., and Xu, B. (2020). Artificial intracellular filaments. Cell Rep. Phys. Sci. 1, 100085.
- 34. Wang, F., Gnewou, O., Modlin, C., Beltran, L.C., Xu, C., Su, Z., Juneja, P., Grigoryan, G., Egelman, E.H., and Conticello, V.P. (2021). Structural analysis of cross α-helical nanotubes provides insight into the designability of filamentous peptide nanomaterials. Nat. Commun. 12, 407.
- Bowerman, C.J., Ryan, D.M., Nissan, D.A., and Nilsson, B.L. (2009). The effect of increasing hydrophobicity on the self-assembly of amphipathic beta-sheet peptides. Mol. Biosyst. 5, 1058–1069.
- 36. Bowerman, C.J., Liyanage, W., Federation, A.J., and Nilsson, B.L. (2011). Tuning β-sheet peptide self-assembly and hydrogelation behavior by modification of sequence hydrophobicity and aromaticity. Biomacromolecules 12, 2735–2745.
- Lee, N.R., Bowerman, C.J., and Nilsson, B.L. (2013). Sequence length determinants for selfassembly of amphipathic β-sheet peptides. Pept. Sci. 100, 738–750.
- Subramaniam, S., Earl, L.A., Falconieri, V., Milne, J.L., and Egelman, E.H. (2016). Resolution advances in cryo-EM enable application to drug discovery. Curr. Opin. Struct. Biol. 41, 194–202.
- 39. Kuhlbrandt, W. (2014). Cryo-EM enters a new era. eLife 3, e03678.
- Shen, H., Fallas, J.A., Lynch, E., Sheffler, W., Parry, B., Jannetty, N., Decarreau, J., Wagenbach, M., Vicente, J.J., Chen, J., et al. (2018). De novo design of self-assembling helical protein filaments. Science 362, 705–709.
- Egelman, E.H. (2000). A robust algorithm for the reconstruction of helical filaments using single-particle methods. Ultramicroscopy 85, 225–234.
- Tsutsumi, M., and Otaki, J.M. (2011). Parallel and antiparallel β-strands differ in amino acid composition and availability of short constituent sequences. J. Chem. Inf. Model 51, 1457–1464.
- 43. Nelson, R., Sawaya, M.R., Balbirnie, M., Madsen, A.O., Riekel, C., Grothe, R., and

- Eisenberg, D. (2005). Structure of the crossbeta spine of amyloid-like fibrils. Nature 435, 773–778.
- Eisenberg, D.S., and Sawaya, M.R. (2017). Structural studies of amyloid proteins at the molecular level. Annu. Rev. Biochem. 86, 69–95.
- 45. Kamtekar, S., Schiffer, J., Xiong, H., Babik, J., and Hecht, M. (1993). Protein design by binary patterning of polar and nonpolar amino acids. Science 262, 1680–1685.
- West, M.W., and Hecht, M.H. (1995). Binary patterning of polar and nonpolar amino acids in the sequences and structures of native proteins. Protein Sci. 4, 2032–2039.
- Xiong, H., Buckwalter, B.L., Shieh, H.M., and Hecht, M.H. (1995). Periodicity of polar and nonpolar amino acids is the major determinant of secondary structure in self-assembling oligomeric peptides. Proc. Natl. Acad. Sci. U S A 92, 6349–6353.
- West, M.W., Wang, W., Patterson, J., Mancias, J.D., Beasley, J.R., and Hecht, M.H. (1999). De novo amyloid proteins from designed combinatorial libraries. Proc. Natl. Acad. Sci. U S A 96, 11211–11216.
- Dou, Y., Baisnée, P.-F., Pollastri, G., Pécout, Y., Nowick, J., and Baldi, P. (2004). ICBS: a database of interactions between protein chains mediated by β-sheet formation. Bioinformatics 20, 2767–2777.
- Mandel-Gutfreund, Y., and Gregoret, L.M. (2002). On the significance of alternating patterns of polar and non-polar residues in beta-strands. J. Mol. Biol. 323, 453–461.
- Salemme, F.R. (1983). Structural properties of protein beta-sheets. Prog. Biophys. Mol. Biol. 42, 95–133.
- Vauthey, S., Santoso, S., Gong, H., Watson, N., and Zhang, S. (2002). Molecular self-assembly of surfactant-like peptides to form nanotubes and nanovesicles. Proc. Natl. Acad. Sci. U S A 99, 5355–5360.
- von Maltzahn, G., Vauthey, S., Santoso, S., and Zhang, S. (2003). Positively charged surfactantlike peptides self-assemble into nanostructures. Langmuir 19, 4332–4337.
- Bucak, S., Cenker, C., Nasir, I., Olsson, U., and Zackrisson, M. (2009). Peptide nanotube nematic phase. Langmuir 25, 4262–4265.
- Castelletto, V., Nutt, D.R., Hamley, I.W., Bucak, S., Cenker, C., and Olsson, U. (2010). Structure of single-wall peptide nanotubes: in situ flow aligning X-ray diffraction. Chem. Commun. (Camb) 46, 6270–6272.
- Middleton, D.A., Madine, J., Castelletto, V., and Hamley, I.W. (2013). Insights into the molecular architecture of a peptide nanotube using FTIR and solid-state NMR spectroscopic measurements on an aligned sample. Angew. Chem. Int. Ed. Engl. 52, 10537–10540.
- 57. Zhao, Y., Wang, J., Deng, L., Zhou, P., Wang, S., Wang, Y., Xu, H., and Lu, J.R. (2013). Tuning the self-assembly of short peptides via sequence variations. Langmuir 29, 13457–13464.
- 58. Zhao, Y., Deng, L., Wang, J., Xu, H., and Lu, J.R. (2015). Solvent controlled structural transition

Matter Article



- of KI4K self-assemblies: from nanotubes to nanofibrils. Langmuir 31, 12975–12983.
- Zhao, Y., Yang, W., Wang, D., Wang, J., Li, Z., Hu, X., King, S., Rogers, S., Lu, J.R., and Xu, H. (2018). Controlling the diameters of nanotubes self-assembled from designed peptide bolaphiles. Small 14, 1703216.
- Cheng, P.-N., Pham, J.D., and Nowick, J.S. (2013). The supramolecular chemistry of β-sheets. J. Am. Chem. Soc. 135, 5477–5492.
- Caspar, D.L., and Klug, A. (1962). Physical principles in the construction of regular viruses. Cold Spring Harb. Symp. Quant Biol. 27, 1–24.
- Chretien, D., Metoz, F., Verde, F., Karsenti, E., and Wade, R.H. (1992). Lattice defects in microtubules: protofilament numbers vary within individual microtubules. J. Cell Biol. 117, 1031–1040.
- Lu, K., Jacob, J., Thiyagarajan, P., Conticello, V.P., and Lynn, D.G. (2003). Exploiting amyloid fibril lamination for nanotube self-assembly. J. Am. Chem. Soc. 125, 6391–6393.
- Narayanan, T., Rüter, A., and Olsson, U. (2021). SAXS/WAXS investigation of amyloid-β(16-22) peptide nanotubes. Front Bioeng. Biotechnol. 9, 654349.
- Nyrkova, I.A., Semenov, A.N., Aggeli, A., and Boden, N. (2000). Fibril stability in solutions of twisted -sheet peptides: a new kind of micellization in chiral systems. Eur. Phys. J. B 17, 481-497
- Rüter, A., Kuczera, S., Stenhammar, J., Zinn, T., Narayanan, T., and Olsson, U. (2020). Tube to ribbon transition in a self-assembling model peptide system. Phys. Chem. Chem. Phys. 22, 18320–18327.

- Zhou, H.-b., and Wang, L. (1996). Chaos in biomolecular dynamics. J. Phys. Chem. 100, 8101–8105.
- 68. Braxenthaler, M., Unger, R., Auerbach, D., Given, J.A., and Moult, J. (1997). Chaos in protein dynamics. Proteins *29*, 417–425.
- Senior, A.W., Evans, R., Jumper, J., Kirkpatrick, J., Sifre, L., Green, T., Qin, C., Židek, A., Nelson, A.W.R., Bridgland, A., et al. (2020). Improved protein structure prediction using potentials from deep learning. Nature 577, 706–710.
- Lupas, A.N., Pereira, J., Alva, V., Merino, F., Coles, M., and Hartmann, M.D. (2021). The breakthrough in protein structure prediction. Biochem. J. 478, 1885–1890.
- Uversky, V.N. (2016). Dancing protein clouds: the strange biology and chaotic physics of intrinsically disordered proteins*. J. Biol. Chem. 291, 6681–6688.
- Choi, U.B., McCann, J.J., Weninger, K.R., and Bowen, M.E. (2011). Beyond the random coil: stochastic conformational switching in intrinsically disordered proteins. Structure 19, 566–576.
- Zhou, J., and Grigoryan, G. (2015). Rapid search for tertiary fragments reveals protein sequence–structure relationships. Protein Sci. 24, 508–524.
- Zhou, J., and Grigoryan, G. (2020). A C++ Library for Protein Sub-structure Search. bioRxiv. 2020.2004.2026.062612.
- Svergun, D., Barberato, C., and Koch, M.H.J. (1995). CRYSOL-a program to evaluate X-ray solution scattering of biological macromolecules from atomic coordinates. J. Appl. Crystallogr. 28, 768–773.

- Mindell, J.A., and Grigorieff, N. (2003). Accurate determination of local defocus and specimen tilt in electron microscopy. J. Struct. Biol. 142, 334–347.
- Tang, G., Peng, L., Baldwin, P.R., Mann, D.S., Jiang, W., Rees, I., and Ludtke, S.J. (2007).
 EMAN2: an extensible image processing suite for electron microscopy. J. Struct. Biol. 157, 38–46.
- Frank, J., Radermacher, M., Penczek, P., Zhu, J., Li, Y., Ladjadj, M., and Leith, A. (1996). SPIDER and WEB: processing and visualization of images in 3D electron microscopy and related fields. J. Struct. Biol. 116, 190–199.
- Egelman, E.H. (2000). A robust algorithm for the reconstruction of helical filaments using single-particle methods. Ultramicroscopy 85, 225–234.
- Scheres, S.H.W. (2012). RELION: implementation of a Bayesian approach to cryo-EM structure determination. J. Struct. Biol. 180, 519–530.
- Sanchez-Garcia, R., Gomez-Blanco, J., Cuervo, A., Carazo, J., Sorzano, C., and Vargas, J. (2020). DeepEMhancer: a deep learning solution for cryo-EM volume post-processing. bioRxiv, 2020.2006.2012.148296.
- Pettersen, E.F., Goddard, T.D., Huang, C.C., Couch, G.S., Greenblatt, D.M., Meng, E.C., and Ferrin, T.E. (2004). UCSF Chimera—a visualization system for exploratory research and analysis. J. Comput. Chem. 25, 1605–1612.
- 83. Emsley, P., Lohkamp, B., Scott, W.G., and Cowtan, K. (2010). Features and development of Coot. Acta Crystallogr. D Biol. Crystallogr. 66, 486–501.